PAPER

Tuning adatom mobility and nanoscale segregation by twin formation and polytypism

View the article online for updates and enhancements.

IOP ebooks™

Bringing you innovative digital publishing with leading voices to create your essential collection of books in STEM research.

Start exploring the collection - download the first chapter of every title for free.

Tuning adatom mobility and nanoscale segregation by twin formation and polytypism

Luca Francaviglia[1] , Gözde Tütüncüoglu[1] , Federico Matteini[1] and Anna Fontcuberta i Morral[1,2]

[1] Laboratoire des Matériaux Semiconducteurs, Institut des Matériaux, École Polytechnique Fédérale de Lausanne, 1015 Lausanne, Switzerland
[2] Institute of Physics, École Polytechnique Fédérale de Lausanne, CH-1015, Switzerland

E-mail: anna.fontcuberta-morral@epfl.ch

Abstract

Nanoscale variations in the composition of an $Al_xGa_{1-x}As$ shell around a GaAs nanowire affect the nanowire functionality and can lead to the formation of localized quantum emitters. These composition fluctuations can be the consequence of variations of crystal phase and/or nanoscale adatom mobility. By applying electron-microscopy-related techniques we correlate the optical, compositional and structural properties at the nanoscale on the same object. The results indicate a clear correlation between the twin density in the nanowire and the quantum-emitter density as well as a significant redshift in the emission. We propose that twinning increases nanoscale segregation effects in ternary alloys. An additional redshift in the emission can be explained by the staggered band alignment between wurtzite and zinc-blende phases. This work opens new avenues in the achievement of homogeneous ternary and quaternary alloys in nanowires and in the engineering of the segregation effects at the nanoscale.

Supplementary material for this article is available online

Keywords: nanowire, quantum dot, polytypism, segregation, cathodoluminescence, transmission electron microscopy

(Some figures may appear in colour only in the online journal)

1. Introduction

Semiconductor nanowires (NWs) and quantum dots (QDs) provide a suitable platform for photodetection and emission at the single-photon and classical level [1–3] as well as for classical and quantum computing [4–8]. In addition, it is well-known that NWs can host crystal phases otherwise unstable in normal conditions in the bulk form. Hexagonal wurtzite (WZ) phase can be achieved both in III–V and group IV semiconductors, which otherwise typically exhibit a cubic zinc-blende (ZB) or diamond phase in the bulk [9–11]. This unique property has allowed to access the WZ GaAs bandgap and the alignment of its band edges with respect to those of the ZB phase [12–16]. In addition to its value in fundamental studies, the tuning of the NW crystal phase is exploited to define QDs

in NWs [17–20]. On the other hand, uncontrolled variations in the crystal phase, along with the existence of stacking defects (through twins and stacking faults) can be detrimental for the functionality of the NWs. Improved optical and electrical properties are demonstrated in defect-free NWs [21, 22].

In addition to a different electronic band structure, WZ and ZB exhibit slightly different surface properties that impact the adatom mobility during growth. The coexistence of WZ, ZB and twins in the same NW is thus an excellent platform to study how the NW crystal phase impacts the adatom incorporation on the NW sidewalls under the same growth conditions [15, 23–25]. Adatom mobility and sticking coefficient determine the formation of radial heterostructures, like core–shell NWs [25]. Here, we study GaAs-$Al_{0.33}Ga_{0.67}As$ core–shell NWs grown by
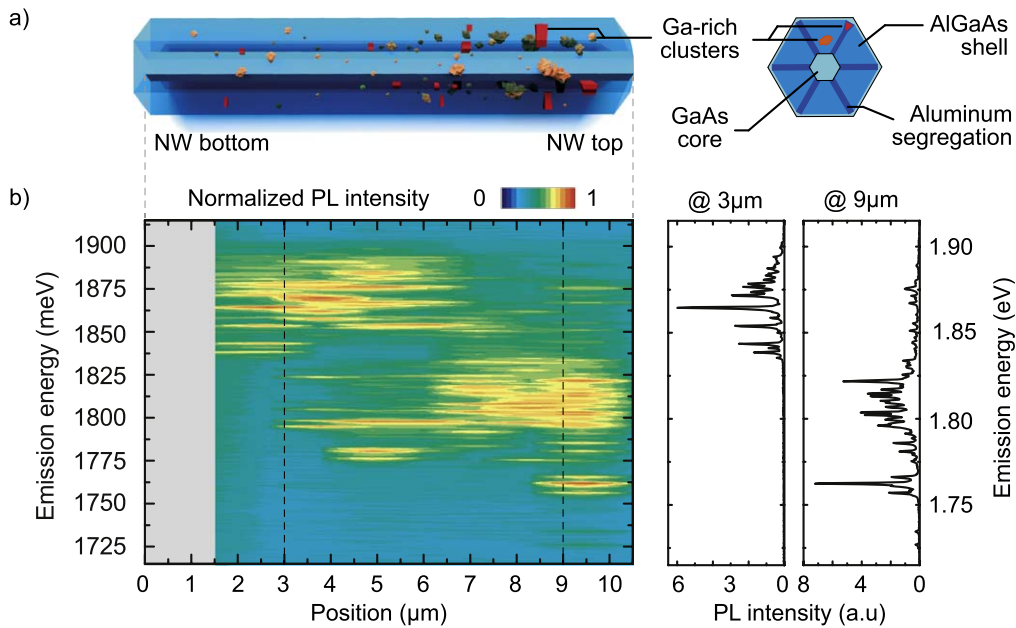
Figure 1. (a) Simplified 3D representation and cross-sectional sketch of the core–shell GaAs-AlGaAs NW structure. The possible Ga-rich emitters are depicted in red and orange in the shell, depicted in blue [26–28]. (b) On the left: contour plot of normalized PL spectra in the 1.72–1.90 eV energy range from the bottom to the top of a NW on a TEM grid (1 μm steps between consequent spectra). The gray band indicates a NW segment covered by the TEM grid carbon film, as revealed by the SEM image in figure 2(c). No emission was detected in this region. On the right: PL spectra (not normalized) from the positions indicated by the dashed vertical lines in the contour plot.

molecular beam epitaxy (MBE). It has been shown that AlGaAs exhibits spontaneous segregation of Al and Ga at the nanoscale. Ga-rich clusters can form [26, 27] and act as QD-like single-photon emitters in the 1.72–1.90 eV emission range [26, 28]. While the exact formation mechanism for these QDs is still unknown, the differentiated adatom mobility in the facets and corners of the NW core is one of the key elements in the explanation.

A sketch of the structure of the studied NWs and NW-based QDs is provided in figure 1(a). In a previous publication [28], we reported on a correlation between the shell thickness and the QD emission energy, which we confirmed also by CL maps (figure S6 in the supporting information, available online at stacks.iop.org/NANO/30/054006/mmedia). Both on large NW ensembles and at the single-NW level, the QDs redshift for an increasing shell thickness, probably because of the occurrence of larger QDs in a thicker shell. However, together with this smooth energy shift related to thickness, a more abrupt decrease of the emission energy was caused by some other factor. In this work, we study the possible role of structural defects in the core to trigger the Ga segregation, providing clues on the QD formation mechanism. In particular, we consider the effect of stacking defects on the electronic band alignment in the QDs and on the self-segregation process that forms the Ga-rich QDs of the shell. We study the optical properties of the QDs on a grid for transmission electron microscopy (TEM) in order to correlate the local emission characteristics at the nanoscale with the information on the structure and the shell composition obtained by electron microscopy. Similarly to the work of Heiss *et al* [13], we study identical NWs by photoluminescence (PL), cathodoluminescence (CL), scanning electron microscopy (SEM), TEM and

energy-dispersive x-ray spectroscopy (EDS). We then provide a simple model to explain and support the experimental data. We first simulate the QD emission energy in function of the density of twins, which alters the band edges of the QD potential well. We then discuss how the crystal phase of the GaAs core can perturb the compositional profile of the (Al) GaAs matrix epitaxially grown around the GaAs core. We recall that the inhomogeneous composition of the NW shell is at the origin of the formation of the NW-based QDs studied in this work. A single factor, the crystal structure of the NW core, has a large impact on the QD optical emission acting on both the semiconductor bandgap and the QD composition itself.

2. Experimental methods

A schematic representation of the structure of our NWs is presented in figure 1(a). We start by growing GaAs NWs by the Ga-assisted method on a (111)Si substrate covered by native oxide as explained in detail in [29, 30]. The NWs have a hexagonal cross-section. Once the GaAs NWs are about 10-μm long, we stop the NW vertical growth by interrupting the Ga supply and consuming the Ga droplet. We switch then to planar epitaxial conditions for {110} surfaces and grow an AlGaAs shell [31]. For the samples investigated here, the Ga and Al deposition rates were set to 0.6 Å s^{-1} and 0.3 Å s^{-1} respectively, which results in the stoichiometry Al$_{0.33}$Ga$_{0.67}$As. Scanning TEM (STEM) EDS measurements indicate an average composition of the NW shell of 27% ± 2%; Raman measurements conduct to a comparable average of 29% ± 8% of Al in the NW shell [32]. The Al shell content has been

extensively reported to be spatially non-uniform, with Al-rich planes at the ridge between two NW facets [26–28, 33]. By changing the deposition time of the AlGaAs shell we grew three different samples with nominal shell thickness of 30 , 50 , and 100 nm. Here, we report on the samples with a 50 nm thick shell. Data on the 30 and 100 nm samples are consistent with the ones on the 50 nm and are shown in figures S5 and S10 in the supporting information. We always complete the AlGaAs shell growth with the deposition of 5 nm of GaAs to avoid oxidation. We transfer few NWs from the three samples onto three different carbon-coated TEM grids by gently scrubbing the grid on the as-grown sample. The observed NWs lie horizontally on one of their six side facets, supported by the carbon film. Markers on the TEM grids facilitate the localization of the same NWs for each of the measurements: PL, SEM-CL, TEM and (S)TEM EDS. For the current work, we perform TEM after the optical characterization in order to avoid the deterioration of the NW optical properties by interaction with accelerated electrons of high energy. Nevertheless, we observe that the NW emission is not affected by long CL mappings. No evidence of e-beam-induced heating is found, therefore no preventive measure is implemented to disperse heat [34]. We perform the PL measurements in a close-loop liquid-helium Attocube cryostat cooled down to 4.2 K. We use a continuous-wave HeNe laser as an excitation source with wavelength equal to 632.8 nm. Through an objective with NA = 0.85, we focus the laser light on the sample in a spot of 1 μm in diameter. The power density at the sample is less than 100 W cm^{-2}. We collect the PL signal through the same objective, disperse it with a 300 l mm^{-1} grating and detect it with a nitrogen-cooled charge-coupled device (CCD). The integration time for each spectrum is 1 s. For PL linescans, the Attocube piezo-positioner ensures the movement along a NW in 1 μm long steps. Together with SEM images, the step distance allows to define the absolute position of the PL spectra on the NW. We perform the CL measurements in an Attolight Rosa SEM-CL microscope. The TEM grids are mounted in the microscope on a stage cooled down to 12 K by liquid-helium. We excite the luminescence with a current in the order of 1 nA and an acceleration voltage of 1.5 kV. This produces a small interaction volume of primary electrons in the NW (figure S1 in the supporting information). A reflective objective (NA 0.71) embedded within the electron optics collects the emitted light to a 32 cm focal-length spectrometer, where a 600 l mm^{-1} grating disperses the signal onto a Peltier-cooled CCD. For each NW, we acquire several 128 × 128 pixels CL maps and merge them into a unique map after the acquisition. The exposure time of each pixel is 100 ms. In the same setup and right before each CL map, we acquire the SEM images of exactly the same sample regions by means of an Everhart-Thornley detector. We use an FEI Tecnai OSIRIS TEM operated at 200 kV (point resolution of 0.24 nm) to study the NW crystal structure, both in conventional bright-field (BF) and high-resolution (HR) TEM modes. We tilt the NWs to observe them along the ZB $\langle 110 \rangle$ direction or equivalent WZ $\langle 11–20 \rangle$, as confirmed by the diffraction patterns. The NW growth direction is $\langle 111 \rangle$. Only the edges of the NWs are thin enough for performing HRTEM without further sample preparation. For this reason we solely show HRTEM micrographs of the shell. However, one should note that the shell grows epitaxially around the GaAs core and its crystal phase follows the structure of the core [25, 35]. We acquire EDS maps in STEM mode in the same microscope at a probe current of 2 nA. The TEM image acquisition relies on a Gatan Orius CCD camera, while four silicon drift detectors at a 0.9-srad solid angle collect the x-ray signal for the compositional mapping. We calculate the QD emission energy by 1D simulations of an 8 nm GaAs potential well with Al$_{0.2}$Ga$_{0.8}$As barriers. We iteratively solve the Poisson and Schrödinger equations by means of the commercially available software Nextnano [36, 37]. The reported exciton energies include the contribution of the charge-carrier confinement and the exciton binding energy. The QD potential well is simplified as pure GaAs in order to use the experimental values in [13] and because the exact band structure of WZ AlGaAs is still a matter of debate [38–40]. The potential barrier is set by Al$_{0.2}$Ga$_{0.8}$As, in agreement with the experimental Al fluctuations in the shell away from the Al-rich ridges [27, 33]. The QD width is chosen in agreement with previous studies [26, 27, 41]. We use the software material parameters for ZB GaAs and AlGaAs, while we overwrote the software library for the WZ GaAs by upshifting the conduction- and valence-band (CB and VB) edges respectively by 53 meV and 76 meV, with respect to ZB [13]. In figure S8 in the supporting information we show more simulations for different WZ band offsets available in the literature, which confirm the findings shown here.

3. Results

Figure 1(b) shows a contour plot of the PL spectra acquired at 1 μm steps from the bottom to the top (increasing NW position) of a GaAs-Al$_{0.33}$Ga$_{0.67}$As core–shell NW. The 3D NW sketch in figure 1(a) is aligned with the PL linescan reported in figure 1(b). The gray band in figure 1(b) indicates a segment with no emission at the very bottom of the NW. This segment is covered by the carbon film of the TEM grid, as later revealed by the SEM image in figure 2(c). Two spectra are extracted from the linescan and are reported on the right in figure 1(b). They correspond to the positions indicated by the vertical dashed lines in the contour plot. In both the extracted spectra and the contour plot, the reported range of the emission energy (1.72–1.90 eV) corresponds to the QD emission. Given the diffraction-limited spatial resolution of PL, the single QDs appear to stretch over few μm in the linescan. Each spectrum in the contour plot is normalized between 0 and 1, in order to primarily appreciate the position in energy of the QD emission. We observe that some lines group together both in space and energy. In particular, one group is visible in the bottom part of the NW at energies between 1.85 and 1.90 eV, while a second one can be found at lower energies (between 1.80 and 1.85 eV) in the top part of the NW. Therefore, the NW results to be divided into two regions according to two groups of different emission energy. In addition to some isolated lines, the two main groups define a
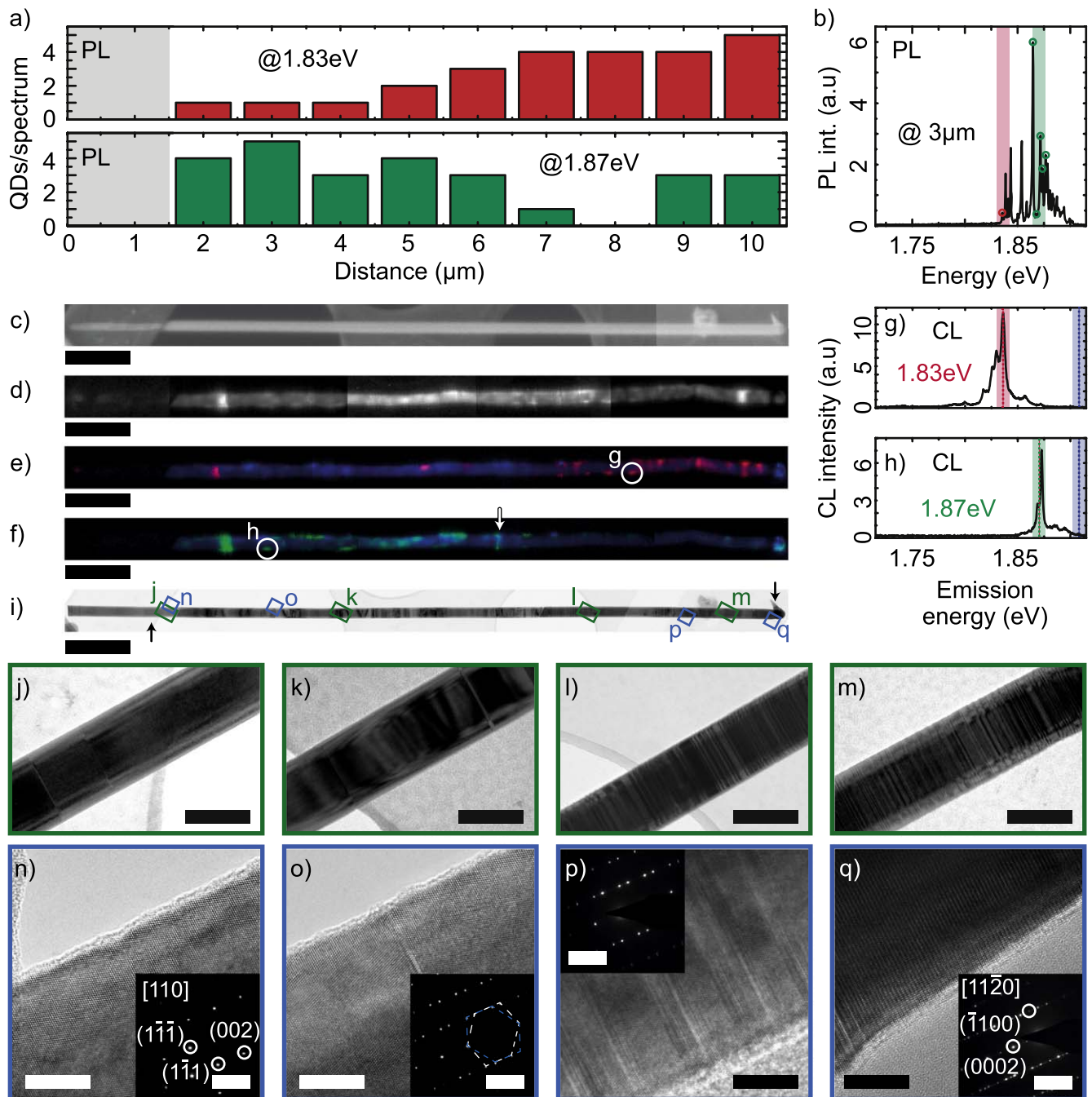
Figure 2. (a) Histograms of the QD occurrence in PL spectra for the two spectral regions centered at 1.83 and 1.87 eV. The data are extracted from the PL spectra shown on the right in figure 1(b) according to the automatic routine described in [28]. (b) Illustrative PL spectrum with indicated the peaks found by the routine (same PL spectrum as the one at 3 μm in figure 1(b)). The red and green stripes respectively correspond to energy ranges centered at 1.830 ± 0.007 eV and 1.870 ± 0.007 eV. (c) SEM image of the same NW. (d) Panchromatic 12 K SEM-CL map of the same NW. (e)–(f) Energy-filtered CL maps of the same NW. Color coding: 1.910 ± 0.007 eV in blue in (e) and (f), 1.830 ± 0.007 eV in red in (e) and 1.870 ± 0.007 eV in green in (f). The arrow in (f) indicates an extended emitter that crosses the entire NW diameter. (g)–(h) Single-pixel CL spectra corresponding, respectively, to the localized emitters circled in (e) and (f). The PL spectra on the right of figure 1(b) were acquired at the same positions. (i) BF-TEM micrograph of the same NW. (j)–(m) Zoomed-in TEM micrographs of different regions along the NW as indicated in figure 2(i). (n)–(q) HRTEM micrographs of the NW at the positions indicated in (i). The diffraction patterns are in the insets in each figure from (n) to (q). Scale bars: (c)–(f), (i) 1 μm, (j)–(m) 200 nm, (n)–(q) 10 nm and 4 nm^{-1} in the insets.

spatially abrupt transition at 7 ± 1 μm. The uncertainty comes from the 1 μm steps of the linescans and the spatial resolution of micro-PL. The comparison of the two selected spectra on the right confirms a redshift of the groups of QD lines when moving towards the NW top. The two spectra also show that more QD lines appear towards the NW top, which reflects an increased amount of optically active QDs. We turn now to a detailed analysis of the spectral features and

statistical occurrence of the QDs along the NW. Figure 2(a) illustrates the occurrence of QD lines per PL spectrum in two selected energy intervals centered at 1.830 ± 0.007 meV (upper red histogram) and 1.870 ± 0.007 meV (lower green histogram). The number of QD lines per spectrum is indicative of the number of QDs per spectrum. Each histogram column corresponds to one PL spectrum. The selection of the QD lines is performed automatically as described in [28]. An example of the QD-peak detection procedure is shown in figure 2(b). We show the PL spectrum at 3 μm (identical to the one reported on the right of figure 1(b)). The red- and green-shaded stripes correspond to the chosen energy intervals and the red and green circles to the selected QD peaks. We note that we chose to monitor the occurrence of the emission at the lower and higher energy range, but that there are other peaks in between these two energies. The plot in figure 2(a) indicates that the number of QDs emitting around 1.83 eV increases from 1 QD/spectrum to 5 QDs/spectrum in the direction of the NW tip. Concomitantly, the occurrence of QDs emitting at 1.87 eV decreases from a maximum of 5 QDs/spectrum at 3 μm from the base to no QDs at 8 μm. Surprisingly, 4 QDs/spectrum appear again in this energy range at the tip of the NW. Yet, the overall count of PL QD lines shows that the low-energy (1.83 eV) emitters become more frequent towards the NW top, while the opposite happens with those emitting at high energy (1.87 eV). We now turn to a higher spatial resolution of the luminescence by providing the CL mapping on the same NW. CL measurements can improve the spatial resolution of luminescence mapping beyond the PL limits. The size of the electron beam, the volume of the exciton generation and the minority-carrier diffusion length define the CL spatial resolution (figure S1 in the supporting information) [42]. In addition, the CL resolution can be improved by selecting only one emission energy range at a time, which may rule out the detection of multiple spatially close emitters. The spectral selection [43] improves the spatial resolution in the energy-filtered CL maps. Figure 2(c) shows the SEM image of the NW. Figure 2(d) corresponds to the panchromatic (all-wavelength) map of the CL emission, where brighter pixels correspond to more intense CL signal. Figures 2(e) and (f) show only selected emission energies from the panchromatic maps. The color coding is the following: 1.910 ± 0.007 eV in blue in both (e) and (f), 1.830 ± 0.007 eV in red in (e) and 1.870 ± 0.007 eV in green in (f). Red and green encode the same energy ranges chosen in figure 2(a). The scale bars in figures 2(c)−(f) correspond to 1 μm. The histograms in figure 2(a) and the CL maps in figures 2(c)–(f) are aligned. The SEM image revealed that the very bottom segment of the NW is covered by a portion of carbon film from the TEM grid. Our measurements indicate that it weakens the signal from this portion of NW with respect to the rest by light absorption and reflection. In all the reported CL maps we can recognize bright emission over the full length of the NW, besides the carbon-covered base. The CL emission at 1.91 eV corresponding to the band-edge emission of AlGaAs (shown in blue) is found through the full NW length. It does not exhibit spatial localization features as for the other emission peaks. On the contrary, the

emitters at 1.83 and 1.87 eV (figures 2(e) and (f) respectively) are clearly spatially localized. The emission zones exhibit different shapes and dimensions. Some extend over very few pixels (each pixel is about 20 × 20 nm), while others are larger and appear as stripes across the full NW diameter. An example is indicated by the arrow in figure 2(f) at about 6 μm from the NW base. Especially in figures 2(e) and (f), SEM-CL allows to clearly resolve localized emitters not only along the NW long axis, but also within the 200 nm thick NW diameter. We recognize the bright and localized emitters in the CL maps as the shell QDs revealed by the PL spectra. This correlation is also corroborated by the similar trend in the occurrence of high- and low-energy emitters in the upper and lower portions of the NW as illustrated here below. The CL mappings of figures 2(e)–(f) clearly illustrate that most of the emission at 1.83 eV stems from the upper part of the NW (above about 7 μm in figure 2(e)). Reversely, the emission at 1.87 eV mainly stems below 7 μm (figure 2(f)), with the exception of a rather large emitter at the very tip of the NW. Interestingly, there are almost no low-energy (1.83 eV) emitters below 7 μm (figure 2(e)). Similarly, the upper region of the NW shows almost no emission at high energy (1.87 eV —figure 2(f)). The transition between the two spectral regions in the CL maps is quite abrupt and in good spatial agreement with the PL linescan (figures 1(b) and 2(a)).

Figure 2(g) reports a single-pixel CL spectrum acquired at about 7 μm on the NW, while figure 2(h) reports a single-pixel CL spectrum acquired at about 3 μm on the NW. These positions are indicated by circles in figures 2(e) and (f) respectively. By comparison with the PL spectra acquired at the same positions, one can observe that the CL spectra are consistent with the PL. In particular, the CL spectrum acquired towards the NW top (figure 2(g)) emits at lower energy than the one acquired in the lower part of the NW (figure 2(h)).

We proceed now to correlate the QD emission characteristics with the local structural properties of the NW. For this, we show the TEM data from the identical NW. Figure 2(i) corresponds to the low-magnification (scale bar 1 μm) BF TEM image of the NW. We use this full length image to locate the position of the higher-magnification TEM images taken from the NW bottom to the top and reported in figures 2(j)−(q), as indicated by the corresponding letters. In particular, figures from 2(j) to (m), framed in green, are BF TEM images at the same intermediate magnification (scale bars equal to 200 nm); figures from 2(n) to (q), framed in blue, are HRTEM images (scale bar 10 nm). The insets in figures 2(n) to (q) are the diffraction patterns (scale bar 4 nm⁻¹) taken at the positions of the corresponding HR micrographs.

In figures 2(j)−(m) we observe brightness contrast as radial stripes along the NW. From the HRTEM micrographs in figures 2(n)−(q) we recognize that this contrast stems from twins in a ZB crystal. We find only one extended WZ segment at the very top of the NW (figure 2(q)). As a general trend valid on few-μm-long NW segments, we quantify less than 20 twins μm^{-1} in the lower part of the NW and about 200 twins μm^{-1} in the upper NW, with an abrupt increase
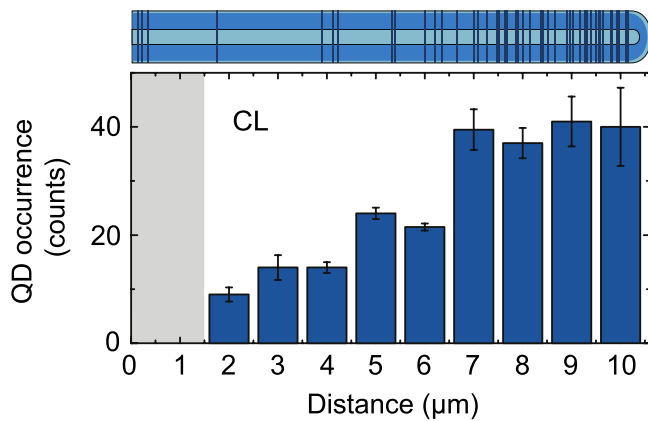
Figure 3. Graph of the QD density (counts per μm) versus NW position. The error bars are the standard deviations of the distributions of QD occurrence in each μm. The gray stripe indicates the NW bottom hidden by the carbon film. A sketch of the twinned NW is aligned above the plot.

above 7 μm (figure S2 in the supporting information). As an illustrative case, figure 2(n) shows a 50 nm NW segment of pure ZB phase at the NW bottom. Moving towards the NW top, more rotational twins are visible: first isolated, like in figure 2(o), then with increasing density, like in figure 2(p). Such a trend in twin density has already been reported for similar GaAs NWs [13]. Excluding the WZ region at the very top of the NW (figure 2(q)), each twin-free segment in the rest of the NW follows the ZB atomic stacking. The plane of a twin between two ZB segments results in a WZ-like atomic stacking [34, 44]. In principle, an increase in twin density can be regarded as an increase in the insertion of WZ planes along the NW. In the upper NW, the density of twins is high and the distance between two defect interfaces can reduce to one lattice constant, that is, the thickness of the defect itself [13]. We move now to the correlation between the QD occurrence and density with the crystalline structure of the NW. CL provides indeed enough spatial resolution to count single bright emitters along the NW. The number of bright QDs visible in the CL as a function of the position along the NW is plotted in figure 3. On top of the graph we include a sketch of the NW with an illustration of the twin density along the axis, as obtained by HRTEM. The data are grouped in 1 μm steps to smoothen the curve and facilitate the reading. The error bars are the standard deviations of the distributions of QD occurrence in each μm. We observe that the lower part of the NW hosts about 20 QDs μm^{-1}. At positions between 7 and 10 μm about 40 QDs μm^{-1} are observed. We thus conclude that, also considering the QD density, the NW seems to be split into two differentiated regions. These, in turn, correlate well with the two regions of different density of twins.

4. Discussion

In the following, we discuss the spatial correlation between (1) the increasing twin density and increasing QD density and (2) the increasing twin density and decreasing QD emission

energy. First, we discard the presence of an average gradient in the NW composition along its main axis. For this, we provide an analysis of the average chemical composition in the shell by EDS STEM. The two black arrows in figure 2(i) indicate the position where we acquired EDS STEM maps (figure S3 in the supporting information). Within the experimental error, there is no difference of Al/Ga average concentration in the two positions, which would affect the shell bandgap along the NW at the microscale [45]. Equally important, we do not observe any variation in the NW diameter, which would hint to a gradient in the shell thickness [28]. We consider two hypotheses: (i) the ZB–WZ band alignment and (ii) the anisotropic deposition of different adatoms on the NW sidewalls. As already mentioned, a rotational twin in ZB can be considered as a WZ plane [46]. Thus, we first address the modification of the band alignment in the QD by the existence of WZ inclusions in a ZB structure, similarly to [13]. In spite of some disagreement about the exact values, it is widely reported in the literature that GaAs WZ and ZB have very similar band gaps at low temperature and a staggered band alignment [12–16, 38, 46]. In particular, both the VB and CB edges are upshifted in WZ, which favors the accumulation of holes in the WZ region and electrons in the ZB. When electrons and holes radiatively recombine across the WZ–ZB interface, the emitted photon is redshifted with respect to both the WZ and the ZB band gaps [12, 13, 38]. This transition is sketched in the inset of the main graph of figure 4. We can consider a similar band alignment in the AlGaAs shell, where twins are the epitaxial continuation of those of the core. The CL data consist of excitation maps of the NW luminescence and the bright emitting stripes that sometimes we observed across the whole NW diameter (see for example the region indicated by the arrow in the CL map in figure 2(f)) can provide evidence of the presence of type-II band alignment in the AlGaAs shell. Their alignment along the NW radial direction suggests a tight link with twins: the twin-induced staggered band alignment in AlGaAs (similar to the one in GaAs) may account for the electron and hole localization at a ZB-WZ interface [12, 46].

Twins epitaxially propagate from the NW core to the shell [35, 47]. A QD is defined by a nanoscale change in the composition of the AlGaAs matrix. Both pure ZB and twins can propagate through the Ga-rich segregations that act as the observed QDs. Given the high density of twins in the upper part of the NW, the occurrence of twins in the crystal structure of a QD is highly probable in this NW region. An increase in the twin density has been correlated with an increased probability of thicker WZ-like segments [13]. We have calculated the exciton recombination energy for several configurations where an increasing amount of thicker WZ segments is included in a QD. The thicknesses are consistent with the HRTEM observations. The alignment of the VB (red) and CB (blue) of these mixed-phase QDs is sketched in figure 4 (the gray bands represent WZ) and overlapped to the calculated hole (red) and electron (blue) density probabilities. We consider configurations ranging from pure ZB to pure WZ. We have ordered them by energy of the exciton (decreasing from
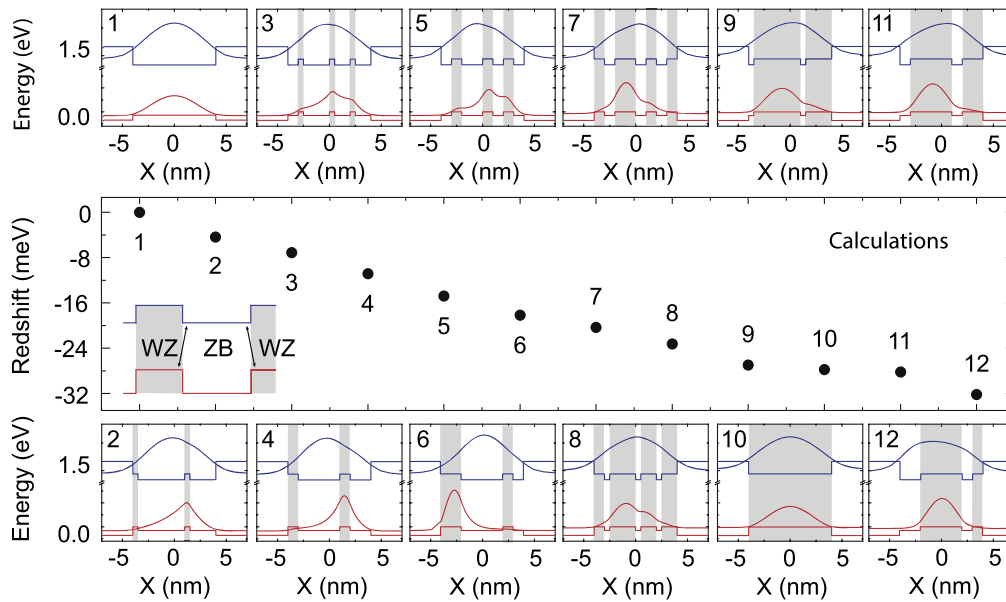
Figure 4. Simulations of the QD exciton emission energy in function of the WZ–ZB ratio and relative arrangement inside the QD. The zero corresponds to the emission energy from the ZB QD. The twelve energies are reported by decreasing energy and linked by their number with sketch of the simulated QD structure, reported above and below the graph. Each sketch shows the CB and VB edges (upper/blue and lower/ red respectively) and the electron and hole density probabilities (upper/blue and lower/red respectively). The gray bands correspond to WZ.

left to right). Each configuration is numbered to help the reader to link it with the energies reported in the main graph in figure 4. The emission energy of the QD of pure ZB is taken as the reference zero (configuration #1).

We first observe that any inclusion of WZ in the QD results in a decrease of the exciton energy, up to a maximum redshift of about 32 meV. In part, this depends on the fact that the WZ bandgap that we used in our simulations is smaller than the ZB one by 23 meV [13]. Yet, this is not the only contribution to the redshift of the exciton energy. This consideration is confirmed by the fact that the pure-WZ QD (configuration #10) has not the most redshifted emission. In addition, the only extended WZ segment experimentally observed at the NW top (figure 2(q)) is not correlated with a local redshift of the QD emission (figures 1 and 2). We rather highlight that the staggered WZ–ZB band alignment plays a key role in the emission energy reduction [12–14, 38]. Such a band alignment localizes electrons and holes in ZB and WZ segments, respectively, which favors their recombination across the ZB–WZ interface. Such a spatially indirect transition is redshifted with respect to the direct recombination at the ZB and WZ band gaps because of the VB and CB offsets. From the density probabilities in figure 4, we qualitatively observe that the carrier localization is more evident in the WZ segments where holes are confined. This is a direct consequence of the larger hole effective mass with respect to electrons. Since the localization of electrons and holes in spatially separated segments is the cause of the redshifted indirect recombination, we conclude the heavy holes take on the main contribution of the emission redshift. We remark that the carrier localization in different regions reduces the exciton binding energy. This results into a blueshift of the emission that is revealed in our simulations (not shown). However, it is

limited to 1 meV at most and is minor if compared to the redshift due to the spatially indirect transitions.

Our simulations clearly point to the fact that a mixed-phase can induce a large redshift of the exciton recombination energy. Nevertheless, the occurrence of a mixed crystal phase has not only an influence on the QD electronic bands. The formation of our QDs relies on the segregation of Al/Ga [33] in a ternary alloy. It is accepted that this should depend on the nature of the NW core facets: (110), (112) as well as the polarity of the latter [48, 49]. Therefore, we have to consider that the crystal phase of the core can directly influence the QD formation and composition, and, as a consequence, the QD occurrence and emission energy. For instance, the facilitation of the QD formation at an early stage of the shell deposition allows each QD cluster to grow larger and emit at lower energies [28]. We highlight that Ga-rich clusters should grow to a diameter of at least 4 nm to contribute to the PL spectra [33]. An evidence that the occurrence of twins may facilitate the QD formation is the increase of the QD density in the upper part of the NW (figure 3), where the twins are significantly denser (from about 7 μm to the top of the NW). Further support to the correlation between defects and segregation comes from the recent observation that Al is preferentially incorporated on the stacking faults and short ZB segments of WZ GaAs-AlGaAs core–shell NWs [50].

In the following, we elaborate on the twin-induced enhancement of the Al/Ga segregation and propose two mechanisms. In a first case, we base our discussion on the fact that, for several material combinations in core–shell NWs, the growth rates of the shell are reported to depend on the core facets, as well as on the crystal phase and the presence of defects in the NW core [23–25, 51–54]. As a result, the shell morphology becomes rough, even in the cases in which the underlying NW facets are originally flat [25]. In particular, the
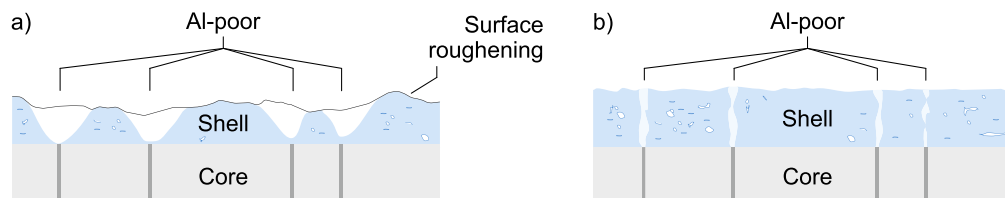
Figure 5. Sketches of the side-view section of core–shell NWs. They illustrate in a cartoon style two scenarios of twin-driven Al–Ga segregation in the NW shell. The core is in gray: darker regions represent twins. The AlGaAs shell is depicted in light-blue: the darker the color, the larger the Al content. (a) Al depletion at the twin positions due to surface roughening. (b) Al depletion at the twin positions driven by different preferential incorporation of Al and Ga on the facets exposed by twin and pure ZB.

positions of discontinuity in the growth rate correspond to the stacking defects [25, 52]. We adapt this scenario to the ternary alloy in our GaAs-AlGaAs NWs. In figure 5(a) we sketch a side view of a NW cross-section: the GaAs core is in gray, with the twins in a darker color; the shell is in blue, with lighter shades corresponding to Al depletion. We depict the shell growth front as irregular: in regularly twinned core–shell NWs with anisotropic shell growth rate, prominent features as high as about 10 nm are observed on the shell surface [25]. A rough shell surface has a variable curvature, which introduces local gradients in the surface chemical potential (μ). We highlight that surface roughness at the atomic scale already defines an uneven μ profile for the adatom diffusion. Therefore, a net flux of different adatoms forms according to the Nernst–Einstein equation and because of the different diffusion lengths of the adatom species involved in the growth (S4 in the supporting information) [55]. In the case of AlGaAs, Ga has a longer diffusion length with respect to Al [56]. We expect that Ga concentrates where the shell is concave because these are the positions where the surface curvature lowers μ. We illustrate this phenomenon in figure 5(a) by showing that Ga enriches the concavities formed on top of the twins (white in the light-blue shell matrix).

We also propose a second mechanism of segregation enhancement in which we neglect the roughening of the NW surface. We propose this scenario to highlight that other factors can alter the NW surface energy. For instance, twins are expected to introduce a different configuration of bonding sites at the surface [57, 58]; similarly, simulations and experiments have shown that the surface energy of the GaAs NW sidewalls depends on the NW crystal phase [15, 24, 58, 59]. Therefore, Al and Ga can be incorporated at a different rate in different positions of flat NW facets according to the presence of twins and WZ or ZB segments. To support this consideration, we remind that Al enrichment has been reported on the stacking faults in WZ GaAs-AlGaAs NWs [50]. In the upper part of our NWs we observed high density of twins in ZB. Therefore, in comparison with [50], we have the opposite phase and we then assume that the formation of Ga-rich clusters is enhanced in the upper part of our NWs. This, in turn, may promote the formation of QD-like emitters. In figure 5(b) we represent the side-view section of a core–shell NW with the same color coding as in figure 5(a). In agreement with our discussion, we depict a flat shell growth front and illustrate that the Al depletion happens at the twin positions (lighter color in the shell).

It is often observed that the sidewalls of twinned NWs are composed of alternated {111}A- and {111}B-type facets rather than the flat {110} type [57]. In our case, like in [50], our measurements cannot prove that the NW facets become atomically rougher in presence of twins and stacking faults. For simplicity, we neglected the surface roughness in the discussion of the second mechanism of segregation enhancement. However, the real case is probably a combination of the two mechanisms: the twins induce a roughening of the NW sidewalls, but also have intrinsically a different surface energy with respect to the surrounding phase. Overall, the twins facilitate the Al/Ga segregation.

Figure 5(b) also suggests an alternative explanation for the bright emission observed across the whole NW diameter in the CL maps (exemplified by the one indicated by the white arrow in figure 2(f)). We already proposed that the WZ–ZB type-II band alignment can propagate into the shell and localize excitons along the NW longitudinal axis. Here, we also consider that Ga-rich rings may form on top of a twinned core and radially grow with the shell. The lower bandgap of Ga-rich rings can confine excitons according to a type-I band alignment. Similar rings were predicted for the Sb segregation on ZB-WZ GaAs NWs [24], while Al-rich rings have been observed in the shell of twinned WZ GaAs-AlGaAs NWs [50].

5. Conclusion

In conclusion, we combined different experimental techniques at high spatial resolution to demonstrate that QD-like Ga-rich clusters in the shell of GaAs-AlGaAs core–shell NWs correlate in occurrence and emission energy with the NW crystal structure. With the support of simulations, we concluded that the band alignment inside a twinned QD redshifts the exciton recombination in agreement with PL and CL observations. We also discussed the further impact of the NW crystal phase on the QD composition and formation during the MBE growth. Our results can apply to other NW systems, where a ternary alloy is grown around a core and alloy segregation is observed [60]. The control of the crystal structure is then crucial to optimize the optical properties of quantum wells (QWs) and QDs obtained on the NW sidewalls [61], acting on their composition and band alignment. Defect-free NW cores guarantee the highest homogeneity in the composition of a NW shell made of a ternary alloy for, e.g. avoiding

exciton localization in a shell QW [62]. Alternatively, by tuning the NW nucleation and growth conditions, several examples in the literature show that it is possible to engineer the insertion of WZ–ZB segments in the NW core [9, 10, 18, 51, 58, 63]. The control of these segments translates into the control of the properties of the shell QDs reported here by promoting their formation and tuning their emission energy. This is in agreement with [50], where segments of alternated crystal phase have been used to locally engineer the shell composition.

Acknowledgments

ORCID iDs

Luca Francaviglia ⓘ https://orcid.org/0000-0002-2138-0837
Gözde Tütüncüoglu ⓘ https://orcid.org/0000-0001-8812-5999
Anna Fontcuberta i Morral ⓘ https://orcid.org/0000-0002-5070-2196

References

[1] Reimer M E *et al* 2011 *J. Nanophoton.* **5** 53502–12
[2] Friedler I, Sauvan C, Hugonin J P, Lalanne P, Claudon J and Gérard J M 2009 *Opt. Express* **17** 2095–110
[3] Munsch M, Malik N S, Dupuy E, Delga A, Bleuse J, Gérard J M, Claudon J, Gregersen N and Mørk J 2013 *Phys. Rev. Lett.* **110** 1–5
[4] Bryllert T, Wernersson L E, Fröberg L E and Samuelson L 2006 *IEEE Electron Device Lett.* **27** 323–5
[5] Thelander C *et al* 2006 *Mater. Today* **9** 28–35
[6] Colinge J P *et al* 2010 *Nat. Nanotechnol.* **5** 225–9
[7] Mourik V, Zuo K, Frolov S M, Plissard S R, Bakkers E P A M and Kouwenhoven L P 2012 *Science* **336** 1003
[8] Lutchyn R M, Bakkers E P, Kouwenhoven L P, Krogstrup P, Marcus C M and Oreg Y 2018 *Nat. Rev. Mater.* **3** 52–68
[9] Glas F, Harmand J C and Patriarche G 2007 *Phys. Rev. Lett.* **99** 3–6
[10] Fontcuberta i M A, Arbiol J, Prades J D, Cirera A and Morante J R 2007 *Adv. Mater.* **19** 1347–51
[11] Lopez F J, Hemesath E R and Lauhon L J 2009 *Nano Lett.* **9** 2774–9
[12] Spirkoska D *et al* 2009 *Phys. Rev.* B **80** 1–9
[13] Heiss M *et al* 2011 *Phys. Rev.* B **83** 1–10
[14] Ketterer B, Heiss M, Uccelli E, Arbiol J and Fontcuberta i M A 2011 *ACS Nano* **5** 7585–92
[15] Hjort M, Lehmann S, Knutsson J, Timm R, Jacobsson D, Lundgren E, Dick K A and Mikkelsen A 2013 *Nano Lett.* **13** 4492–8
[16] Geijselaers I, Lehmann S, Dick K A and Pistol M E 2018 *Nano Futures* **2** 035002
[17] Akopian N, Patriarche G, Liu L, Harmand J C and Zwiller V 2010 *Nano Lett.* **10** 1198–201
[18] Krogstrup P, Popovitz-Biro R, Johnson E, Madsen M H, Nygård J and Shtrikman H 2010 *Nano Lett.* **10** 4475–82
[19] Pemasiri K *et al* 2009 *Nano Lett.* **9** 648–54
[20] Vainorius N, Lehmann S, Jacobsson D, Samuelson L, Dick K A and Pistol M E 2015 *Nano Lett.* **15** 2652–6
[21] Dalacu D, Mnaymneh K, Lapointe J, Wu X, Poole P J, Bulgarini G, Zwiller V and Reimer M E 2012 *Nano Lett.* **12** 5919–23
[22] Thelander C, Caroff P, Plissard S, Dey A W and Dick K A 2011 *Nano Lett.* **11** 2424–9
[23] Xu T, Dick K A, Plissard S, Nguyen T H, Makoudi Y, Berthe M, Nys J P, Wallart X, Grandidier B and Caroff P 2012 *Nanotechnology* **23** 095702
[24] Hjort M, Kratzer P, Lehmann S, Patel S J, Dick K A, Palmstrøm C J, Timm R and Mikkelsen A 2017 *Nano Lett.* **17** 3634–40
[25] Gorji G S, Heurlin M, Wernersson L E, Lehmann S and Dick K A 2012 *Nanotechnology* **23** 285601
[26] Heiss M *et al* 2013 *Nat. Mater.* **12** 439–44
[27] Mancini L *et al* 2014 *Appl. Phys. Lett.* **105** 243106
[28] Francaviglia L, Fontana Y, Conesa-Boj S, Tütüncüoğlu G, Duchêne L, Tanasescu M B, Matteini F and i Morral A F 2015 *Appl. Phys. Lett.* **107** 033106
[29] Colombo C, Spirkoska D, Frimmer M, Abstreiter G and Fontcuberta i M A 2008 *Phys. Rev.* B **77** 155326
[30] Matteini F, Tütüncüoğlu G, Potts H, Jabeen F and Fontcuberta i M A 2015 *Cryst. Growth Des.* **15** 3105–9
[31] Heigoldt M, Arbiol J, Spirkoska D, Rebled J M, Conesa-Boj S, Abstreiter G, Peiró F, Morante J R and Fontcuberta i M A 2009 *J. Mater. Chem.* **19** 840–8
[32] Francaviglia L, Giunto A, Kim W, Romero-Gomez P, Vukajlovic-Plestina J, Friedl M, Potts H, Güniat L, Tütüncüoglu G and Fontcuberta i M A 2018 *Nano Lett.* **18** 2393–401
[33] Jeon N, Loitsch B, Morkoetter S, Abstreiter G, Finley J, Krenner H J, Koblmueller G and Lauhon L J 2015 *ACS Nano* **9** 8335–43
[34] Bao J *et al* 2008 *Nano Lett.* **8** 836–41
[35] Algra R E, Hocevar M, Verheijen M A, Zardo I, Immink G G W, Van Enckevort W J P, Abstreiter G, Kouwenhoven L P, Vlieg E and Bakkers E P A M 2011 *Nano Lett.* **11** 1690–4
[36] Trellakis A, Zibold T, Andlauer T, Birner S, Smith R K, Morschl R and Vogl P 2006 *J. Comput. Electron.* **5** 285–9
[37] Birner S, Zibold T, Andlauer T, Kubis T, Sabathil M, Trellakis A and Vogl P 2007 *IEEE Trans. Electron Devices* **54** 2137–42
[38] De A and Pryor C E 2010 *Phys. Rev.* B **81** 155210
[39] Funk S, Li A, Ercolani D, Gemmi M, Sorba L and Zardo I 2013 *ACS Nano* **7** 1400–7
[40] Yeh C Y, Wei S H and Zunger A 1994 *Phys. Rev.* B **50** 2715–8
[41] Fontana Y, Corfdir P, Van Hattem B, Russo-Averchi E, Heiss M, Sonderegger S, Magen C, Arbiol J, Phillips R T and Fontcuberta i M A 2014 *Phys. Rev.* B **90** 075307
[42] Yacobi B G and Holt D B 1986 *J. Appl. Phys.* **59** R1–24
[43] Kumar Balla N, Rendón-Barraza C, Hoang L M, Karpinski P, Bermúdez-Ureña E and Brasselet S 2017 *ACS Photonics* **4** 292–301
[44] Birman J L 1959 *Phys. Rev.* **115** 1493–505
[45] Chen C, Shehata S, Fradin C, LaPierre R, Couteau C and Weihs G 2007 *Nano Lett.* **7** 2584–9
[46] Rudolph D, Schweickert L, Morkötter S, Hanschke L, Hertenberger S, Bichler M, Koblmüller G, Abstreiter G and Finley J J 2013 *New J. Phys.* **15** 113032

[47] Conesa-Boj S, Hauge H I, Verheijen M A, Assali S, Li A, Bakkers E P and Fontcuberta i M A 2015 *Nano Lett.* **15** 2974–9

[48] Zheng C, Wong-Leung J, Gao Q, Tan H H, Jagadish C and Etheridge J 2013 *Nano Lett.* **13** 3742–8

[49] Petroff P, Cho A, Reinhart F, Gossard A and Wiegmann W 1982 *Phys. Rev. Lett.* **48** 170–3

[50] Jeon N, Ruhstorfer D, Döblinger M, Matich S, Loitsch B, Koblmüller G and Lauhon L 2018 *Nano Lett.* **18** 5179–85

[51] Dick K A, Thelander C, Samuelson L and Caroff P 2010 *Nano Lett.* **10** 3494–9

[52] Kawaguchi K, Heurlin M, Lindgren D, Borgstrm M T, Ek M and Samuelson L 2011 *Appl. Phys. Lett.* **99** 97–100

[53] Wallentin J, Messing M E, Trygg E, Samuelson L, Deppert K and Borgström M T 2011 *J. Cryst. Growth* **331** 8–14

[54] Rieger T, Luysberg M, Schäpers T, Grützmacher D and Lepsa M I 2012 *Nano Lett.* **12** 5559–64

[55] Biasiol G and Kapon E 1998 *Phys. Rev. Lett.* **81** 2962–5

[56] Koshiba S, Nakamura Y, Tsuchiya M, Noge H, Kano H, Nagamune Y, Noda T and Sakaki H 1994 *J. Appl. Phys.* **76** 4138–44

[57] Caroff P, Dick K A, Johansson J, Messing M E, Deppert K and Samuelson L 2009 *Nat. Nanotechnol.* **4** 50–5

[58] Pankoke V, Kratzer P and Sakong S 2011 *Phys. Rev.* B **84** 1–8

[59] Rosini M and Magri R 2010 *ACS Nano* **4** 6021–31

[60] Sköld N, Wagner J B, Karlsson G, Hernán T, Seifert W, Pistol M E and Samuelson L 2006 *Nano Lett.* **6** 2743–7

[61] Zamani M *et al* 2018 *Nanoscale* **10** 17080

[62] Chomette A, Deveaud B, Regreny A and Bastard G 1986 *Phys. Rev. Lett.* **57** 1464–7

[63] Yuan X, Caroff P, Wong-Leung J, Fu L, Tan H H and Jagadish C 2015 *Adv. Mater.* **27** 6096–103